Simulations of a Multipinhole SPECT Collimator for Clinical Dopamine Transporter (DAT) Imaging

Arda Könik, Jan De Beenhouwer, Joyeeta M. Mukherjee, Kesava Kalluri, Soumyanil Banerjee, Navid Zeraatkar, Timothy Fromme, and Michael A. King

***Abstract*—SPECT imaging of the dopamine transporter (DAT) is used for diagnosis and monitoring progression of Parkinson's disease (PD), and differentiation of PD from other neurological disorders. The diagnosis is based on the DAT binding in the caudate and putamen structures in the striatum. We previously proposed a relatively inexpensive method to improve the detection and quantification of these structures for dual-head SPECT by replacing one of the fan-beam collimators with a specially designed multipinhole (MPH) collimator. In this paper, we developed a realistic model of the proposed MPH system using the GATE simulation package and verified the geometry with an analytic simulator. Point source projections from these simulations closely matched confirming the accuracy of the pinhole geometries. The reconstruction of a hot-rod phantom showed that 4.8-mm resolution is achievable. The reconstructions of the XCAT brain phantom showed clear separation of the putamen and caudate, which is expected to improve the quantification of DAT imaging and PD diagnosis. Using this GATE model, point spread functions modeling physical factors will be generated for use in reconstruction. Also, further improvements in geometry are being investigated to increase the sensitivity of this base system while maintaining a target spatial resolution of 4.5–5 mm.**

***Index Terms*—Brain, multipinhole (MPH), simulation, SPECT.**

I. Introduction

SPECT imaging of the dopamine transporter (DAT) is used for diagnosis and monitoring progression of Parkinson's disease (PD), and differentiation of PD from other neurological disorders with similar clinical presentations. The diagnostic evaluation is made visually and/or semiquantitatively from the reconstructed images, which present DAT binding in the caudate and putamen. These small structures (nuclei) within the striatum lie in the central region of the brain. Imaging of the occipital cortex, is also required for the semiquantitative approaches using the striatal binding ratio (SBR), a measure of striatal specific binding, relative to the nonspecific binding in the occipital cortex. Thus, SBR is calculated as (STR−OCC)/OCC, where STR and OCC are the activity concentrations estimated in the striatum and occipital cortex, respectively [1]. Caudate-to-putamen ratio (CPR) is another potentially useful measurement since parkinsonian syndromes tend to affect the caudate nucleus and putamen with different severity [2].

DAT imaging is typically performed with a general-purpose parallel-beam (or fan-beam) SPECT scanner. The limited spatial resolution provided by these systems (7–10 mm) is often not sufficient for accurate segmentation of putamen and caudate, potentially introducing errors into the quantitative interpretation, especially for CPR calculation or other studies operating in smaller regions within the striatum [3]. Thus, a dedicated brain SPECT system focusing on the striatum could be an ideal imaging solution to improve the resolution and sensitivity tradeoff.

One of the earliest dedicated brain imaging SPECT systems employed multipinhole (MPH) coded apertures in a lead-alloy hemispherical shell providing a system resolution of 8.7 mm and sensitivity of 0.024% at the center of the field of view (FOV) [4]. A full-ring MPH system provided 3.3-mm resolution at 0.017% sensitivity or 8-mm resolution at 0.102% sensitivity [5]. An annular SPECT system consisting of a three-segment parallel-beam rotating collimator within a stationary annular crystal (CeraSPECT) provided 8.3-mm resolution and 0.022% sensitivity at the central axis [6], [7]. The collimators of this system were replaced with variable focusing collimators (SensOgrade) to further increase the sensitivity (by a factor of 1.4–2) [8]. A slit/slat collimator, offered a resolution of 6 mm and sensitivity of 0.051% at the center of the FOV with 35% multiplexing [9]. G-SPECT of MILabs, a stationary MPH system, reported to have a better than 3-mm reconstructed system spatial resolution [10].

The cost of such dedicated systems, however, may be prohibitive for most clinics considering the relatively low number of procedures performed for brain imaging. Therefore, we proposed a relatively inexpensive approach to improve the performance of the existing dual-head SPECT systems for DAT imaging by using a specially designed MPH collimator on one detector head while keeping the existing fan-beam (or parallel-beam) collimator on the other head [11]. With this combined MPH/fan-beam system we aim for improved

Manuscript received January 19, 2018; revised March 17, 2018; accepted April 25, 2018. Date of publication April 30, 2018; date of current version August 31, 2018. This work was supported by the National Institute Biomedical Imaging and Bioengineering under Grant NIH R01-EB022092. A preliminary version of this paper was published in the Proceedings of the IEEE NSS/MIC 2014 by A Könik *et al.*, "Simulations of a combined fan-beam and multi-pinhole SPECT system for clinical I-123 DaTscan imaging," [25], [40], and [41]. This paper significantly refines and extends the preliminary results presented there. *(Corresponding author: Arda Könik.)*

A. Könik, K. Kalluri, S. Banerjee, N. Zeraatkar, and M. A. King are with the Department of Radiology, UMass Medical School, Worcester, MA 01655 USA (e-mail: arda.konik@umassmed.edu).

J. De Beenhouwer is with the imec-Vision Laboratory, University of Antwerp, 2000 Antwerp, Belgium.

J. M. Mukherjee is with MathWorks, Inc., Natick, MA 01760 USA.

T. Fromme is with Robotics Engineering, Worcester Polytechnic University, Worcester, MA 01609 USA.

Color versions of one or more of the figures in this paper are available online at http://ieeexplore.ieee.org.

Digital Object Identifier 10.1109/TRPMS.2018.2831208

detection and quantification of structures in the interior region of the brain at a marginal cost. The MPH collimator provides enhanced spatial resolution and system sensitivity within the interior of the brain. The fan-beam collimator provides lower resolution, but complete sampling of the brain, addressing data sufficiency and allowing SBR calculation over the occipital cortex. The design goal for the MPH component is to obtain a reconstructed resolution of 4.5–5 mm in the striatum region allowing caudate and putamen differentiation for calculation of CPR. The improved resolution of these structures offers new potentials for the diagnosis of PD as the syndromes tend to affect the caudate and putamen with different severity [2] and the binding in the posterior putamen was reported to be a better indicator for early diagnosis of PD [12], [13].

Other combined systems have been proposed for brain imaging employed mainly a combination of cone-beam (or half-cone-beam)/parallel-hole [14]–[17] and half-cone-beam/fan-beam collimators [18] on triple-head SPECT systems. A combined single-pinhole/parallel-hole SPECT system for diagnosis of ischemia was also proposed [19]. A combined fan-beam/cone-beam approach was developed for dual-head SPECT systems [20]. Recently, the cone-beam part of this system was modified to include a slant-hole region to get additional coverage outside the central brain [21] achieving 5.2 times greater overall sensitivity than that of a dual-low-energy high-resolution (LEHR) system at a similar resolution.

Among the other inexpensive approaches for brain imaging based on the modification of an existing system, one example is a brain loft-hole collimator insert for SPECT imaging with an aperture shutter mechanism designed to fit into an existing PET system [22]. Another approach using 20 apertures shows the possibility of increasing the sensitivity by about 21 times over the parallel-hole collimation but severely compromising the spatial resolution [23]. Most recently, two MPH collimators (standard and high-resolution) were proposed to replace the collimators of a dual-head SPECT system [24].

A unique advantage of the MPH usage for DAT imaging is the negligible amount of down-scatter ($\sim$2%) from the low-abundance high-energy photons of the ^{123}I ($>$500 keV) as opposed to $>$25% reported for conventional collimators through real experiments and simulations [25], [26]. The reason for such low down-scatter in MPH is because of the solid aperture plate (except where the pinholes are present) stopping the high-energy photons much more effectively than the conventional collimators with very large number of holes. For the same reason, higher primary-to-penetration and primary-to-scatter ratios can be expected with the usage of MPH.

An accurate simulation model of the MPH system is essential for design investigation and optimization. Apart from the geometric aspects of the pinhole imaging such as resolution, sensitivity, magnification, and FOV, the selection of the collimator material and thickness is also important considering high-energy photon penetration and scatter effects for ^{123}I imaging. An accurate simulation model is also needed for the development of reconstruction software using point spread functions (PSFs) that include physical factors such as collimator penetration, intrinsic spatial resolution, and depth of interaction (DOI), which are especially important for obliquely oriented pinholes. Therefore, a realistic model of the proposed MPH system using the GATE Monte Carlo simulation package [27] was developed. The implementation of the MPH geometry in GATE involves challenging constructs such as oblique pinholes formed by back-to-back alignment of trapezoid volumes. Unlike most MPH systems, the apertures in this design are not parallel to the crystal surface (except for the direct pinhole) complicating the PSFs, entrance/exit ports and hence the detector coverage. To confirm the accuracy of the geometry, the same MPH system was modeled with an independent analytic simulator. In this paper, we present the analytic verification of the GATE geometry through simulations of various activity distributions.

II. Methods

A. Design and Simulation Geometry of the MPH Collimator

For the initial test of the MPH/fan-beam approach, the Philips BrightView SPECT system was considered with an active detector area of 54×40 cm^2 and a 0.9525 cm NaI(Tl) scintillation crystal thickness. The fan-beam collimator of this system was already simulated in GATE [28] and verified with analytic simulations [29]. Therefore, this paper focuses on the simulations of the MPH component of the combined system. The geometric variables such as collimator thickness, magnification, pinhole aperture sizes, positions, and tilt angles were fully parameterized to facilitate testing of different potential configurations. The simulations are based on the MPH design as described in [11]: a tungsten alloy collimator plate ($20 \times 20 \times 2$ cm^3) containing nine knife-edge pinholes (one direct and eight oblique angles), with 2.2-mm square apertures at 0.5-cm depth from the face of the collimator plate (on the side closer to the brain), all focusing to the same central point. Image magnification of this system at the focal point is $\sim$1.2, with the aperture center to crystal distance of 17.25 cm and axis of rotation (AOR) to aperture distance of 14 cm. With this configuration, a cylindrical volume of interest (VOI) of $\sim$12-cm diameter by $\sim$8-cm height could be imaged without multiplexing. The system was designed to provide a spatial resolution of 4.7 mm including 3-mm intrinsic resolution and geometric sensitivity of 0.013% at the center of the VOI.

The GATE implementation of the MPH geometry is illustrated in Fig. 1, where the pinholes are formed by the back-to-back alignment of symmetric-trapezoids focusing on the center of the cylindrical VOI. The trapezoid volumes were generated at the aperture center (x_o, y_o, z_o) and rotated by an angle $\alpha = \tan^{-1}((\hat{x}^2 + \hat{y}^2)^{1/2}/\hat{z})$ orienting them to the focal point, where $(\hat{x}, \hat{y}, \hat{z})$ are the components of the aperture normal $(\hat{n})$ pointing to the focal point; and the rotation axis $(\hat{y}, -\hat{x}, 0)$, is parallel to collimator plane and perpendicular to the $\hat{x}$ and $\hat{y}$ components of the normal vector. Next, the two volumes were translated in the opposite directions along the focal axis by half of their height H. That is, $(\pm H\hat{x} - x_o, \pm H\hat{y} - y_o, \pm H\hat{z} - z_o)/2$. We used 10^{-10} mm precision for these translation values to avoid volume overlaps between the oblique trapezoids (air) and collimator (tungsten).

In this base MPH configuration, the pinholes are organized symmetrically about the middle column (pinholes 2, 5, and 8). The most oblique pinholes (1 and 3) are tilted by 43° relative

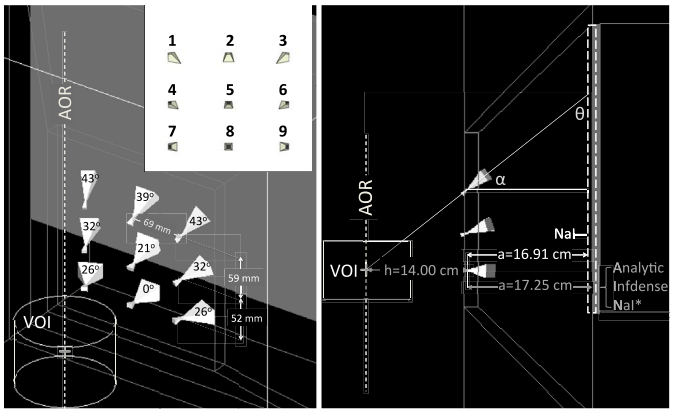

(a) (b)

Fig. 1. (a) MPH geometry implemented in GATE showing one direct and eight oblique pinholes (tilt angles are labeled), all focusing to the center of VOI. The insert shows the front view of the collimator plate presenting the shape of the entrance ports and pinhole numbering. (b) Axial view. For the NaI simulations, the crystal (dashed lines) is placed 0.34 cm (GATE measured average DOI) closer to the aperture to approximately maintain the aperture to detection distance of 17.25 cm as in the original design. Analytic, Infdense, and NaI* simulations used $a = 17.25$ cm, however, on average the detection occurs further away for NaI* (at 17.59 cm from the aperture).

to the focal axis of the direct pinhole (8). All the pinhole entrance/exit ports were in irregular shapes except for the direct pinhole with the rectangular ports.

B. Analytic and GATE Simulations

The analytic simulations were based on a geometric ray-tracing method without modeling any physical effects and the detector coverage of each pinhole were predefined nonoverlapping rectangular regions. In contrast, GATE detector coverage varied depending on the size and shape (intersection of the pinhole trapezoid volume and the collimator plane) of the entrance and exit ports of the individual pinholes. GATE simulations were based on the 159-keV primary photon emissions of ^{123}I only (high-energy emissions were not simulated) and no attenuation phantom was included to allow better comparison between GATE and analytic simulations. All relevant photon interactions (i.e., photoelectric effect, Rayleigh scatter, and Compton scatter) were included in the collimator plate, shielding, and crystal. The analytic and three different types of GATE simulations performed in this paper are summarized below.

1) Analytic simulation models the geometry of the MPH design without modeling the physical factors such as attenuation, scatter, DOI, and collimator penetration.
2) GATE Infdense simulation models an idealized system similar to the analytic simulation by using an extremely dense material for the main components (i.e., crystal, collimator, and shield) and perfect energy resolution, thereby virtually eliminating Compton scatter in the photopeak window.
3) GATE NaI* simulation shares the exact same geometry as analytic and Infdense, as shown in Fig. 1(b). This simulation models the photon interactions in the components of the system and results in an average magnification larger than intended because the photons are distributed within the NaI(Tl) crystal (i.e., DOI effect). For these simulations, a 10% detector energy resolution was modeled and the energy window was set 15% symmetrically about the 159-keV photopeak (i.e., 147–171 keV).
4) GATE NaI simulation represents the most realistic and closest system to that of the original design. It accounts for the DOI and approximately matches the original design with the crystal positioned 0.34 cm (average DOI as determined from GATE simulation) closer to the aperture, as indicated in Fig. 1(b). The same detector energy resolution and photopeak window were used as in GATE NaI*.

Projections of the point sources were obtained using all the simulation types detailed above. For the rest of the activity distributions, only the analytic and GATE NaI simulations were performed to obtain 30 equally separated projections over 360°. These projections were then reconstructed using a voxel-driven ordered-subset expectation maximization (OSEM) algorithm, originally developed by Dey [30]. The geometric component of resolution is included in this analytic code followed by the methodology of [31]. The reconstructions of the noise-free analytic projections represented the ideal case as the reconstruction method employed the same forward projector that was used in producing the analytic projection data. The reconstructions of the GATE NaI projections with this analytic projector were less accurate since the projector did not employ PSFs accounting for physical factors. To control the noise in reconstructions of the GATE simulations with low count levels, a post-Gaussian filter was applied. No filter was applied to the rest of the reconstructions, which were either noise-free analytic or high-count GATE simulations.

C. Point Source Simulations

Point source simulations were performed to confirm the correct implementation of the pinhole positions and orientations. Noise-free analytic and low-count GATE Infdense projections of a 2-D grid of point source (size: 11×9 and step: 1 cm) were obtained for an overall PSF comparison within the VOI. In addition, for more detailed PSF analyses, high-count projections of the focal point source and an off-centered source were obtained with the GATE simulations (Infdense, NaI*, and NaI). The projections were in high-resolution (matrix size: 1080×800 and pixel size: 0.5 mm) to allow accurate resolution measurements. In Fig. 2, the focal point source PSFs for the analytic and GATE simulations are shown with and without modeling the detector intrinsic spatial resolution.

D. Sensitivity Theory and Measurements

The geometric sensitivity and the sensitivity measurements (counts from the PSFs) were obtained for the focal point and off-centered point sources. The geometric sensitivity (efficiency) of an aperture can be described as the ratio of the photon flux through the aperture to the total isotropic photon flux emitted by a point source assuming all the photons passing through the aperture are detected. This ratio is approximately equivalent to the area of the aperture plane divided by the surface area of the sphere centered at the point source and tangent to the aperture. For clarification, a lateral view of the MPH is illustrated in Fig. 3(a), where the spherical surface

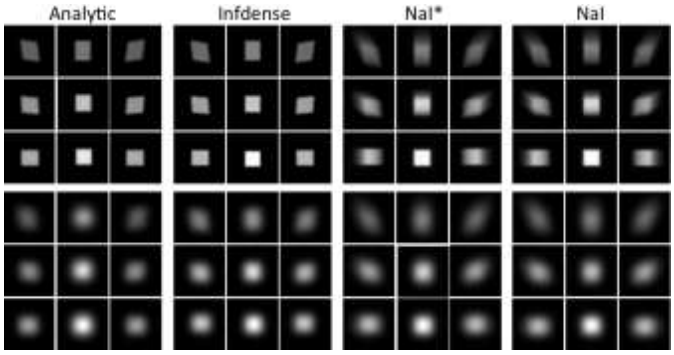

Fig. 2. High-resolution projections of a focal point source (set of nine PSFs) for the analytic and GATE simulations. GATE Infdense used an extremely high-density material for the crystal. GATE NaI* and NaI used the standard NaI(Tl) crystal. The upper four sets of PSFs are from simulations without modeling the intrinsic detector resolution. The lower four sets of PSFs were post-smoothed with an isotropic Gaussian function of 3 mm FWHM modeling the intrinsic detector resolution.

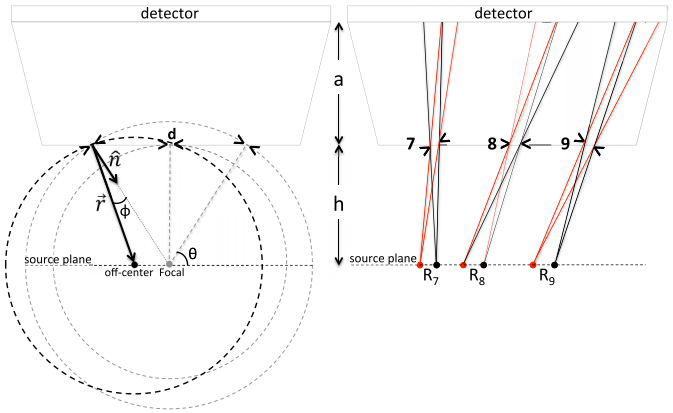

Fig. 3. Lateral view of the MPH is sketched. (a) Circles tangent to the apertures represents the isotropic photon emission. (b) Resolution for the direct pinhole (pinhole 8) is constant (R_8) for a given source plane as the aperture and detector planes are parallel. For the oblique pinholes, the resolution depends on the source location and tilt angle. In this example, pinholes 7 and 9 have the same absolute tilt angles, but source locations are different resulting in different resolutions ($R_7 < R_9$).

(drawn as circle) tangent to the respective aperture represents the isotropic photon emission at distance $|\boldsymbol{r}|$ from the point source. Thus, for the knife-edge pinholes with square apertures, the sensitivity can be expressed as $g = d^2\sin(\theta)/4\pi|\boldsymbol{r}|^2$ or $g = d^2\sin^3(\theta)/4\pi h^2$ [32], where d is the aperture size, θ is the angle between source-to-aperture vector and the source plane, $|\boldsymbol{r}|$ is the magnitude of this vector, and h is the distance between the aperture center and the source plane, as indicated in Fig. 3. For the focal point source, the equation becomes $g = d^2\sin^2(\theta)/4\pi h^2$ for all the nine pinholes since their focusing axes are perpendicular to their aperture planes and for the direct pinhole it reduces to $g = d^2/4\pi h^2$. A more general expression to describe the sensitivity of any source location and aperture tilt angle can be obtained as $g = d^2(\boldsymbol{r}\cdot\widehat{\boldsymbol{n}})/4\pi r^3 = d^2\cos\phi/4\pi|\boldsymbol{r}|^2$ (adapted from [33]), which reduces back to $g = d^2/4\pi|\boldsymbol{r}|^2$ or $g = d^2\sin^2(\theta)/4\pi h^2$ for the focal point. Therefore, for the geometric sensitivity calculations, this general form was used and compared with the sensitivity measurements obtained from the simulations.

E. Spatial Resolution Theory and Measurements

A simple equation for the spatial resolution can be expressed as $R = (R_g^2 + R_i^2/M^2)^{1/2}$ [34], where $R_g = d(1 + 1/M)$ is the geometric term; $M = a/h$ is the magnification factor; and R_i is the detector intrinsic resolution. This equation is valid when the collimator and detector planes are parallel to each other resulting in constant resolution for any point in the source plane. For the tilted apertures, however, the resolution depends on the source location and aperture tilt angle. As illustrated in Fig. 3(b), the resolution of the direct pinhole is uniform (R_8) for any point at the source plane, whereas oblique pinholes, which have the same absolute tilt angles, can have different object resolutions ($R_7 < R_9$) because of the different source positions relative to the apertures. For the MPH system described here, the oblique pinholes are rotated in different axes further complicating a general analytic description for the geometric resolution term.

The resolution measurements were obtained as the full widths at half maximum (FWHMs) of the PSFs in horizontal and vertical directions. For the NaI* and NaI simulations, the built-in GATE detector intrinsic resolution model was enabled and set to 3 mm. The analytic simulations did not have such a built-in function. Hence, the raw PSFs were obtained first and then were post-smoothed with an isotropic Gaussian function to approximately model the 3-mm intrinsic detector resolution. Same method was followed for the GATE Infdense simulations so that they can be compared to the analytic simulations under the same conditions. The FWHMs were then divided by M to obtain the FWHMs in the object space.

F. Cylindrical Source Simulations and Reconstruction

Simulations of the 12-cm diameter by 8 cm in height target cylindrical VOI were performed to investigate the ability of the MPH to reconstruct activity throughout the VOI. For this purpose, the projections were obtained for the noise-free analytic and high-count (23 M detected counts) GATE NaI simulations for 30 equally separated views over 360°. The projections were then reconstructed using 60 OSEM iterations with six subsets (subset size of 5). The same projections served as the background projections for the hot-rod source phantoms described in the next section.

G. Hot-Rod Source Simulations and Reconstruction

Simulations of a hot-rod source phantom, a smaller version of the Deluxe Jaszczak Phantom (data spectrum) fitting in the target cylinder VOI, were performed to estimate the reconstructed resolution of the MPH system. The phantom consisted of six segments of different rod diameters (4.8, 6.4, 7.9, 9.5, 11.1, and 12.7 mm) as in the Deluxe Jaszczak Phantom, but with shorter rods (8 cm instead of 8.8 cm). The rod-source activity concentration was eight times larger than the background concentration (i.e., rod-source:background=8:1), similar to that of a DAT brain image [35]. The noise-free analytic and high-count GATE projections (source: 28 M and background: 23 M) of this phantom were then reconstructed using 60 OSEM iterations with six subsets (subset size of 5).

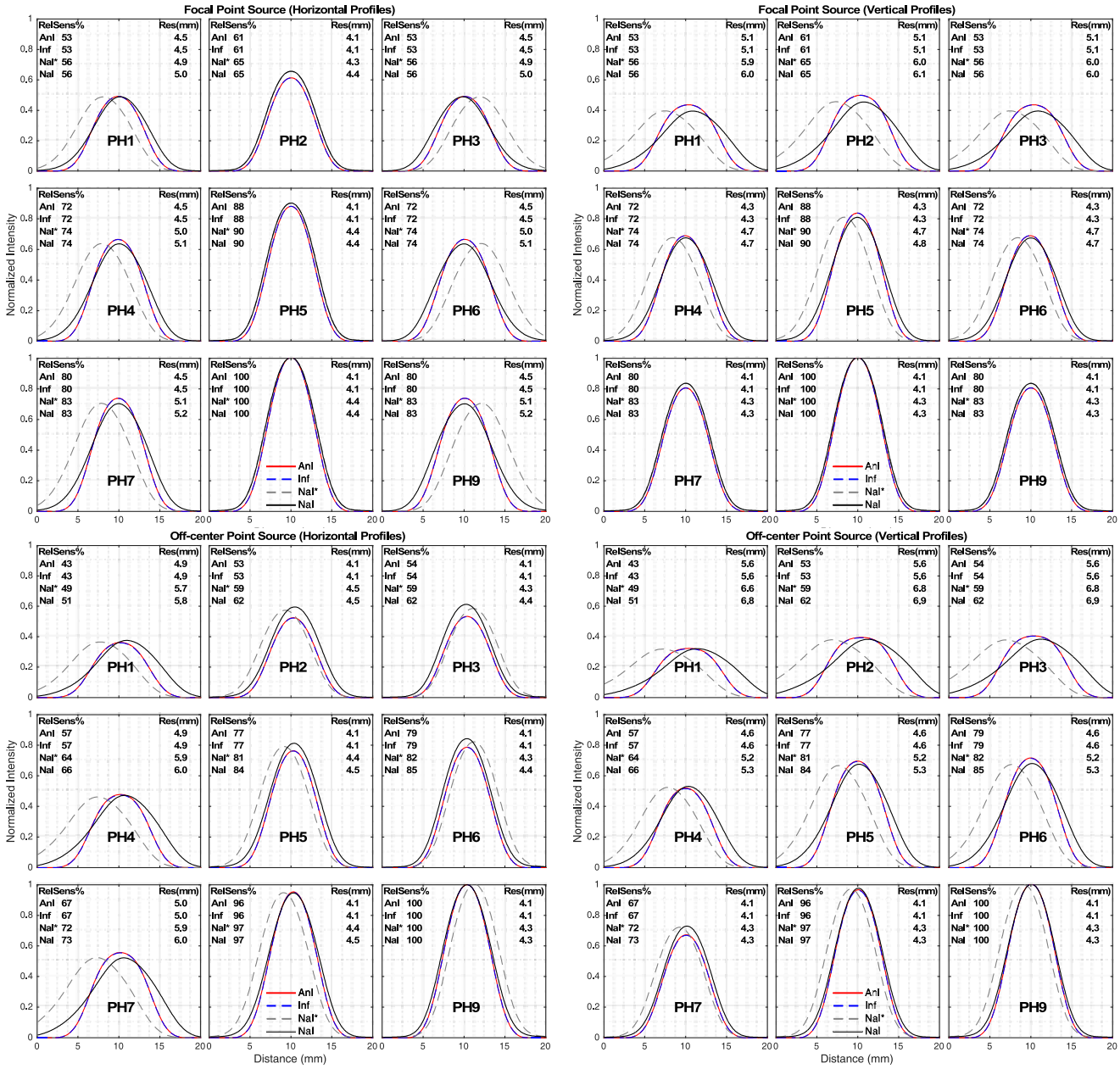

Fig. 4. Normalized horizontal and vertical profiles of the focal (top) and off-center (bottom) point source projections for the analytic (Anl), Infdense (Inf), NaI*, and NaI simulations. The relative sensitivities (RelSens%) were normalized to the projection with the highest sensitivity (number 8 for focal and number 9 for off-centered source). The object resolutions (Res) were calculated from FWHM/M, where M is the magnification factor.

H. XCAT Brain Simulations and Reconstruction With MPH

Projections of the XCAT brain phantom [36] modeling DAT brain imaging were obtained with the striatum: background activity ratio of 8:1. Again the analytic simulations were noise-free representing an ideal case. For the GATE simulations, high-count (10 M) and realistic-count (0.68 M) projections were obtained. A realistic count level (∼6 M) was determined from the average counts measured in 45 clinical DaTscan studies conducted with a three-headed LEHR-fan-beam SPECT system over 40 min of acquisition time. A total count ratio of LEHR-fan-beam: MPH = 2.92:1 was estimated from GATE simulations of these two collimators on the same brain phantom. Therefore, for the realistic simulations of the MPH with 2.2-cm aperture size, 6 M counts/ (3 heads $\times 2.92$) = 0.68 M counts/head was used. For the reconstruction of the noise-free analytic and high-count GATE data 40 OSEM iterations and for the realistic-count GATE 20 OSEM with six subsets (subset size of 5) were used.

III. Results

A. Point Source Profiles

The analytic and GATE Infdense projections were closely aligned for all the grid points (11×9 cm^2, 1 cm spacing). Two of these point sources, the focal and the off-center, were used in the PSF analyses. The analytic and GATE (Infdense, NaI*, and NaI) projections of these two points were post-smoothed with an isotropic Gaussian of 3-mm FWHM to approximately

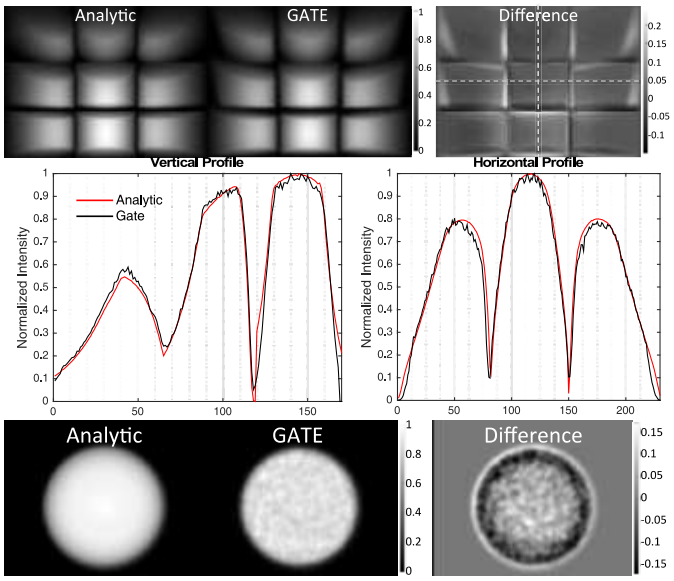

Fig. 5. Top: analytic and GATE projections of the cylindrical source with uniform activity. Middle: central vertical and horizontal line profiles. Bottom: reconstructions of the central slice and the difference image (analytic-GATE). The differences at the boundaries are mainly due to the definition of detection coverage and physical factors (e.g., penetration, scatter, and DOI) included in GATE.

TABLE I
ABSOLUTE VALUE OF DIFFERENCE: MEAN, MINIMUM–MAXIMUM

	[a]Position (mm)	[b]Resolution (mm)	[c]Relative Sensitivity%
	Focal Point Source		
Analytic	–	–	0.0, 0 – 0
Infdense	0.2, 0.0 – 0.7	0.0, 0.0 – 0.0	0.0, 0 – 0
NaI*	1.7, 0.5 – 2.5	0.5, 0.2 – 0.9	2.4, 0 – 4
NaI	0.6, 0.0 – 0.7	0.5, 0.2 – 1.0	2.4, 0 – 4
	Off-center Source		
Analytic	–	–	0.0, 0 – 0
Infdense	0.0, 0.0 – 0.0	0.0, 0.0 – 0.0	0.0, 0 – 0
NaI*	2.2, 1.4 – 3.2	0.6, 0.2 – 1.2	4.1, 0 – 7
NaI	0.5, 0.0 – 1.1	0.6, 0.2 – 1.3	6.0, 0 – 9

[a]Absolute value of difference in position between analytic and GATE
[b]Absolute value of difference in resolution between analytic and GATE
[c]Absolute value of difference in relative sensitivity between theory and simulations

model the intrinsic detector resolution. Horizontal and vertical profiles obtained from the PSFs are shown in Fig. 4. Along with these profiles, relative sensitivity (RelSens%) and resolution (Res) of the PSFs are also displayed. The layout of the profiles follows the pinhole positions as illustrated in Fig. 1(a). For example, the profiles for the direct pinhole (number 8) are placed at the middle of the bottom row. The sensitivities were normalized to the projection with the highest sensitivity, which occurs for the pinhole closest to the source. Thus, the sensitivity plots for the focal point source [Fig. 4(top)] and the off-centered point source [Fig. 5(bottom)] were normalized to that of direct pinhole and pinhole 9, respectively. Table I summarizes the quantitative differences between the analytic and GATE profiles (in both horizontal and vertical directions) in position (based on the index of the maximum value), resolution, and relative sensitivity for focal and off-center sources. Analytic and Infdense results were identical for all these cases except for the focal point source which exhibits a maximum

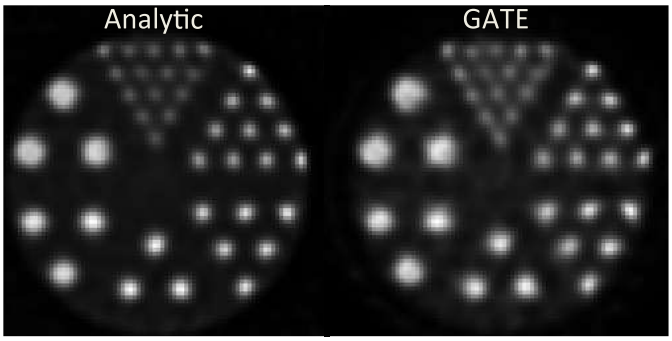

Fig. 6. Noise-free analytic and high-count (51 M) GATE reconstructions of the hot-rod phantom (rod-source:background = 8:1) with six segments of different rod diameters (4.8, 6.4, 7.9, 9.5, 11.1, and 12.7 mm). The smallest segment in GATE slice was resolved in the absence of any resolution and PSF modeling in the reconstruction.

position difference of 0.7 mm, and may be related to the noise in the data or an error in digitization. Also, the theoretical sensitivity calculations matched exactly the measured sensitivities of the analytic and Infdense. Measurements obtained from the NaI* simulations, not accounting for the DOI, were shifted in position (up to 2.5 mm for the focal point source and 3.2 mm for the off-center source). The maximum positional error dropped to 1.1 mm for the NaI simulations as the DOI effect was accounted.

The absolute system sensitivity (detected counts/emitted counts) for the focal point source obtained from the GATE Infdense simulation and the geometric system sensitivities (theory and analytic simulations) matched exactly at 0.013%, whereas the absolute system sensitivity from the GATE NaI simulation dropped to 0.011% due to the limited stopping power and 10% energy resolution of the NaI crystal.

B. Cylindrical Source Projections and Reconstructions

The normalized projections, line profiles, and reconstructions obtained from the analytic and GATE simulations of the cylinder source covering the VOI are shown in Fig. 5. The differences observed in the images and profiles were mainly at the boundaries since the analytic pinholes project to the predefined nonoverlapping rectangular regions, whereas GATE pinhole projections are defined by the irregular shapes of the exit/entrance ports as shown in Fig. 1(b). Other known factors contributing to the differences were collimator penetration and scatter, DOI, and noise in the GATE data.

C. Hot-Rod Phantom Reconstructions

Fig. 6 shows the analytic and GATE NaI reconstructed slices of the hot-rod phantom. The analytic reconstruction represented the ideal case since the projections were noise-free and also the reconstruction software employed the same forward projector that was used in producing the analytic projection data. The image quality in GATE reconstructions was degraded due to the physical effects and noise in the data. Nevertheless, the reconstruction from the high-count GATE projections appears to be well aligned with the analytic reconstruction and resolves the segment with the smallest rods (diameter: 4.8 mm), confirming that the target reconstructed resolution within the VOI is achievable.

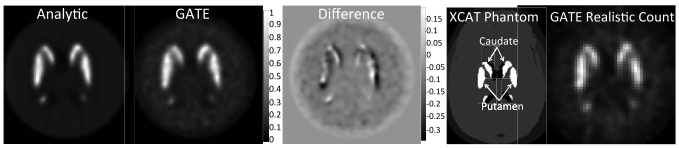

Fig. 7. Noise-free analytic and high-count (10 M) GATE reconstructed slices of the XCAT brain phantom and their difference (analytic-GATE) are shown for the striatum region. The striatal components are labeled on the XCAT phantom for reference. The last image shows the same GATE simulated reconstructed slice at realistic count levels (0.68 M).

D. XCAT Brain Phantom Reconstructions

Fig. 7 shows the reconstructed slices obtained from the analytic and GATE projections of the XCAT brain phantom acquired with the MPH system (2.2-mm square apertures). The first sets of images show the analytic and high-count GATE reconstructions and their difference image. The last image shows the same reconstructed slice at the realistic count levels.

IV. Discussion

The analytic and GATE simulations of the MPH collimator were presented for various phantoms: point sources, a uniform cylinder source, a hot-rod phantom, and the XCAT brain phantom modeling DAT uptake distribution.

The point source projections and their profiles confirmed that the analytic and GATE geometries, most importantly, pinhole positions and orientations were in agreement. While making a direct pinhole from two back-to-back trapezoids (or cones) in GATE is straightforward, the oblique pinholes can be challenging because of the volume overlap problem in GATE. That is, even a very minor volume overlap can lead to unpredictable outcomes in the simulation. Therefore, for the oblique pinholes, the directional cosines were used to define the coordinates of the volumes (trapezoid) with a ten-digit precision (i.e., 10^{-10} mm). With five-digit precision, the shape of the analytic and GATE PSFs were noticeably different and the sensitivities were not matching. Once the higher precision was used in the volume positions, PSF shapes and sensitivities matched exactly. The sensitivities obtained from the geometric equation also matched these PSF measured values for all nine pinholes and for both point sources (focal point and off-center) tested. The GATE NaI accounting for the DOI effect represented the simulation setup closest to the reality including most of the relevant physical factors. Considering the differences between the analytic and GATE NaI simulations, a remarkable agreement was obtained between the two setups. The relative sensitivities (normalized to the maximum pinhole sensitivity) of the NaI were larger than that of analytic and Infdense for all the oblique pinholes. This is expected as the photon path increases within the crystal, the detection efficiency increases for NaI, but it remains the same for the analytic and Infdense as their detection occurs at the crystal surface. In contrary, the absolute system sensitivity for the NaI (0.011%) was smaller than that of analytic and Infdense (0.013%) due to the limited stopping power and 10% energy resolution compared to the ideal crystal.

The reconstructions of the noise-free analytic projections provided the ideal case since the same forward projector was employed in both projection and reconstruction processes. The reconstructions of the GATE NaI projections were degraded since analytic projector did not employ PSFs or account for the physical factors (e.g., penetration and DOI). Nevertheless, simulations of the base MPH configuration with 2.2-mm square apertures showed that 4.8-mm rods are resolved and caudate and putamen were differentiated. Now that a reliable GATE model for the MPH has been created, PSFs can be obtained from the GATE simulations once a final design is reached. With the inclusion of PSF modeling in the reconstruction algorithm further improvement in the resolution can be expected.

The analytic and GATE simulations were fully parameterized for easy implementation of different pinhole geometries. Therefore, while the base MPH design was the main focus of this paper, further design improvements are being investigated. Currently, the pinholes have an axial symmetry, which was useful for initial testing. However, better axial and angular samplings could be obtained by slightly altering the pinhole positions so that each pinhole provides a unique view. Better resolution and higher sensitivity is achieved if the apertures are made closer to the patient head by usage of a body contouring orbit, at the expense of reduced FOV and increased penetration. A curved collimator plate can be also considered to bring the apertures closer to the brain. The overall sensitivity of the MPH could be further increased while maintaining the resolution level, through additional pinholes and implementation of demultiplexing techniques [37]. Also resolution modeling in the reconstruction could enable the usage of larger apertures to improve sensitivity [38]. Finally, the usage of circular apertures as opposed to square ones would be more suitable for modeling the point spread function [39].

In comparing our approach to that of other systems for brain imaging, the base MPH configuration using 2.2-mm square apertures presented here provides a 4.7-mm system spatial resolution in the center of the cylindrical VOI and slightly better sensitivity than LEHR collimators, which will be further improved as mentioned above. For example, in a separate study we showed that the total counts for the MPH using circular apertures of 3 mm is 1.75 times larger than the total counts of the single LEHR fan-beam, which resulted in reasonable putamen and caudate differentiation even without any resolution and PSF modeling in the reconstruction [40]. With multiplexing, the sensitivity of this system can be improved by another 1.75 times as reported in [41].

Future work will investigate ways of improving the sensitivity while maintaining a target spatial resolution (4.5–5 mm) with incorporating PSFs obtained from GATE simulations in the reconstruction algorithm. Using this GATE model, the effect of higher energy photons, task-based optimization of aperture size, multiplexing, and improved axial sampling will be also investigated.

V. Conclusion

An accurate and fully parameterized GATE simulation of the MPH system was developed and the geometry was verified against an independent analytic simulator through projections

of a grid of point sources and uniform activity in the cylindrical VOI. The MPH reconstruction of analytic and GATE projections were in agreement for a uniform cylinder phantom, a hot-rod phantom, and an XCAT brain phantom modeling DAT imaging. The reconstruction of the hot-rod phantom indicated that 4.8-mm resolution is achievable even in the absence of PSF modeling. Also, the MPH/fan-beam reconstructions of the XCAT phantom showed the separation of the caudate and putamen at realistic count levels, which offers new potentials for the diagnosis of PD.

ACKNOWLEDGMENT

The contents are solely the responsibility of the authors and do not necessarily represent the official views of the National Institutes of Health.

REFERENCES

[1] P. H. Kuo *et al.*, "Receiver-operating-characteristic analysis of an automated program for analyzing striatal uptake of 123I-ioflupane SPECT images: Calibration using visual reads," *J. Nucl. Med. Technol.*, vol. 41, no. 1, pp. 26–31, Mar. 2013.

[2] T. A. Soderlund *et al.*, "Value of semiquantitative analysis for clinical reporting of 123I-2-β-carbomethoxy-3β-(4-iodophenyl)-N-(3-fluoropropyl)nortropane SPECT studies," *J. Nucl. Med.*, vol. 54, no. 5, pp. 714–722, May 2013.

[3] C. Vriend *et al.*, "Reduced dopamine transporter binding predates impulse control disorders in Parkinson's disease," *Movement Disord.*, vol. 29, no. 7, pp. 904–911, Jun. 2014.

[4] R. K. Rowe *et al.*, "A stationary hemispherical SPECT imager for three-dimensional brain imaging," *J. Nucl. Med.*, vol. 34, no. 3, pp. 474–480, 1993.

[5] M. C. Goorden, M. C. Rentmeester, and F. J. Beekman, "Theoretical analysis of full-ring multi-pinhole brain SPECT," *Phys. Med. Biol.*, vol. 54, no. 21, pp. 6593–6610, Nov. 2009.

[6] S. Genna and A. P. Smith, "The development of ASPECT, an annular single crystal brain camera for high efficiency SPECT," *IEEE Trans. Nucl. Sci.*, vol. 35, no. 1, pp. 654–658, Feb. 1988.

[7] F. Zito, A. Savi, and F. Fazio, "CERASPECT: A brain-dedicated SPECT system. Performance evaluation and comparison with the rotating gamma camera," *Phys. Med. Biol.*, vol. 38, no. 10, pp. 1433–1442, 1993.

[8] G. El Fakhri, J. Ouyang, R. E. Zimmerman, A. J. Fischman, and M. F. Kijewski, "Performance of a novel collimator for high-sensitivity brain SPECT," *Med. Phys.*, vol. 33, no. 1, pp. 209–215, 2006.

[9] S. T. Mahmood, K. Erlandsson, I. Cullum, and B. F. Hutton, "Design of a novel slit-slat collimator system for SPECT imaging of the human brain," *Phys. Med. Biol.*, vol. 54, no. 11, pp. 3433–3449, Jun. 2009.

[10] F. J. Beekman *et al.*, "G-SPECT-I: A full ring high sensitivity and ultra-fast clinical molecular imaging system with <3mm resolution," presented at the EANM, 2015, p. 1.

[11] M. A. King *et al.*, "Design of a multi-pinhole collimator for I-123 DaTscan imaging on dual-headed SPECT systems in combination with a fan-beam collimator," *IEEE Trans. Nucl. Sci.*, vol. 63, no. 1, pp. 90–97, Feb. 2016.

[12] K. L. Chou *et al.*, "Diagnostic accuracy of [99mTc]TRODAT-1 SPECT imaging in early Parkinson's disease," *Parkinsonism Related Disord.*, vol. 10, no. 6, pp. 375–379, Aug. 2004.

[13] D. J. Brooks, "Imaging approaches to Parkinson disease," *J. Nucl. Med.*, vol. 51, no. 4, pp. 596–609, Apr. 2010.

[14] C. D. Stone, M. F. Smith, K. L. Greer, and R. J. Jaszczak, "A Combined half-cone beam and parallel hole collimation system for SPECT brain imaging," *IEEE Trans. Nucl. Sci.*, vol. 45, no. 3, pp. 1219–1224, Jul. 1998.

[15] M. Defrise and R. Clack, "Filtered backprojection reconstruction of combined parallel beam and cone beam SPECT data," *Phys. Med. Biol.*, vol. 40, no. 9, pp. 1517–1537, Sep. 1995.

[16] R. J. Jaszczak, J. Li, H. Wang, and R. E. Coleman, "Three-dimensional SPECT reconstruction of combined cone beam and parallel beam data," *Phys. Med. Biol.*, vol. 37, no. 3, pp. 535–548, Mar. 1992.

[17] H. Ye, A. Krol, E. D. Lipson, and D. H. Feiglin, "Implementation of a fully 3D iterative reconstruction of combined parallel-and cone-beam collimator SPECT," in *Proc. IEEE NSS/MIC*, Honolulu, HI, USA, 2007, pp. 3501–3504.

[18] R. Ter-Antonyan *et al.*, "Combination of converging collimators for high-sensitivity brain SPECT," *J. Nucl. Med.*, vol. 50, no. 9, pp. 1548–1556, 2009.

[19] Q. Huang, T. Zeniya, H. Kudo, H. Iida, and G. T. Gullberg, "High resolution brain imaging with combined parallel-hole and pinhole collimation," in *Proc. IEEE NSS/MIC*, Knoxville, TN, USA, 2010, pp. 3145–3148.

[20] M. A. Park, S. C. Moore, and M. F. Kijewski, "Brain SPECT with short focal-length cone-beam collimation," *Med. Phys.*, vol. 32, no. 7, pp. 2236–2244, Jul. 2005.

[21] M. A. Park *et al.*, "Introduction of a novel ultrahigh sensitivity collimator for brain SPECT imaging," *Med. Phys.*, vol. 43, no. 8, p. 4734, 2016.

[22] K. Van Audenhaege, S. Vandenberghe, K. Deprez, B. Vandeghinste, and R. Van Holen, "Design and simulation of a full-ring multi-lofthole collimator for brain SPECT," *Phys. Med. Biol.*, vol. 58, no. 18, pp. 6317–6736, 2013.

[23] T. C. Lee *et al.*, "Multipinhole collimator with 20 apertures for a brain SPECT application," *Med. Phys.*, vol. 41, no. 11, Nov. 2014, Art. no. 112501.

[24] L. Chen, B. M. W. Tsui, and G. S. P. Mok, "Design and evaluation of two multi-pinhole collimators for brain SPECT," *Ann. Nucl. Med.*, vol. 31, no. 8, pp. 636–648, Oct. 2017.

[25] A. Könik, J. D. Beenhouwer, and M. A. King, "Advantage of pinhole collimators over parallel hole collimators in reducing downscatter for I-123 imaging," in *Proc. IEEE NSS/MIC*, San Diego, CA, USA, 2015, pp. 1–4.

[26] A. Cot *et al.*, "Study of the point spread function (PSF) for 123I SPECT imaging using Monte Carlo simulation," *Phys. Med. Biol.*, vol. 49, no. 14, pp. 3125–3316, Jul. 2004.

[27] S. Jan *et al.*, "GATE: A simulation toolkit for PET and SPECT," *Phys. Med. Biol.*, vol. 49, no. 19, pp. 4543–4561, Oct. 2004.

[28] J. De Beenhouwer, B. Pieters, and R. Van de Walle, "Fast GATE fan beam SPECT projector," in *Proc. IEEE NSS/MIC*, Valencia, Spain, 2011, pp. 4188–4191.

[29] J. M. Mukherjee *et al.*, "Fast shift-variant resolution compensation within iterative reconstruction for fan-beam collimator," in *Proc. IEEE NSS/MIC*, Orlando, FL, USA, 2009, 3230–3234.

[30] J. Dey, "Improvement of performance of cardiac SPECT camera using curved detectors with pinholes," *IEEE Trans. Nucl. Sci.*, vol. 59, no. 2, pp. 334–347, Apr. 2012.

[31] B. Feng *et al.*, "Modeling of the point spread function by numerical calculations in single-pinhole and multipinhole SPECT reconstruction," *IEEE Trans. Nucl. Sci.*, vol. 57, no. 1, pp. 173–180, Feb. 2010.

[32] J. R. Mallard and M. J. Myers, "The performance of a gamma camera for the visualization of radioactive isotope in vivo," *Phys. Med. Biol.*, vol. 8, pp. 165–182, Jun. 1963.

[33] M. Gieles, H. W. A. M. de Jong, and F. J. Beekman, "Monte Carlo simulations of pinhole imaging accelerated by kernel-based forced detection," *Phys. Med. Biol.*, vol. 47, no. 11, pp. 1853–1867, Jun. 2002.

[34] S. D. Metzler and R. Accorsi, "Resolution-versus sensitivity-effective diameter in pinhole collimation: Experimental verification," *Phys. Med. Biol.*, vol. 50, no. 21, pp. 5005–5017, Nov. 2005.

[35] J. C. Dickson *et al.*, "The impact of reconstruction method on the quantification of DaTSCAN images," *Eur. J. Nucl. Med. Mol. Imag.*, vol. 37, no. 1, pp. 23–35, Jan. 2010.

[36] W. P. Segars, G. Sturgeon, S. Mendonca, J. Grimes, and B. M. Tsui, "4D XCAT phantom for multimodality imaging research," *Med. Phys.*, vol. 37, no. 9, pp. 4902–4915, Sep. 2010.

[37] S. C. Moore *et al.*, "Iterative demultiplexing of multiple-pinhole SPECT projection data," in *Proc. IEEE NSS/MIC*, 2015, p. 7.

[38] P. Aguiar *et al.*, "Analytical, experimental, and Monte Carlo system response matrix for pinhole SPECT reconstruction," *Med. Phys.*, vol. 41, no. 3, Mar. 2014, Art. no. 032501.

[39] J. M. Mukherjee *et al.*, "Stepwise linear regression modeling of the point spread functions of a multi-pinhole SPECT camera for I-123 DaTscan imaging," in *Proc. IEEE NSS/MIC*, Strasbourg, France, 2016, pp. 1–3.

[40] A. Könik *et al.*, "Optimization of pinhole aperture size of a combined MPH/fanbeam SPECT system for I-123 DAT imaging," in *Proc. IEEE NSS/MIC*, Strasbourg, France, 2016, pp. 1–2.

[41] A. Könik *et al.*, "Preliminary investigation of multiplexed pinholes with circular apertures and elliptical ports for I-123 DAT imaging," in *Proc. IEEE NSS/MIC*, 2017, p. 7.